Physics Letters A 373 (2009) 2137–2145

Contents lists available at ScienceDirect

Physics Letters A

www.elsevier.com/locate/pla

Extreme waves that appear from nowhere: On the nature of rogue waves

N. Akhmediev [a], J.M. Soto-Crespo [b,*], A. Ankiewicz [a]

[a] Optical Sciences Group, Research School of Physics and Engineering, The Australian National University, Canberra, ACT 0200, Australia
[b] Instituto de Óptica, C.S.I.C., Serrano 121, 28006 Madrid, Spain

ARTICLE INFO

Article history:
Received 30 March 2009
Accepted 8 April 2009
Available online 17 April 2009
Communicated by V.M. Agranovich

ABSTRACT

We have numerically calculated chaotic waves of the focusing nonlinear Schrödinger equation (NLSE), starting with a plane wave modulated by relatively weak random waves. We show that the peaks with highest amplitude of the resulting wave composition (rogue waves) can be described in terms of exact solutions of the NLSE in the form of the collision of Akhmediev breathers.

1. Introduction

The one-dimensional self-focusing nonlinear Schrödinger equation (NLSE) is a model which approximates the wave dynamics in the ocean [1–8]. Indeed, before trying to understand the results of simulations for two-dimensional equations [9] it is worthwhile to gain a more detailed understanding of what is happening within the one-dimensional model. This may be an easier task, since the NLSE model is completely integrable and all solutions can be analyzed within the framework of the inverse scattering technique, or at least at a qualitative level based on our understanding of NLSE solutions.

The importance of modulation instability in creating ocean waves was noticed by Peregrine [10]. Small amplitude waves may grow to higher amplitudes if their frequencies are within the frequency band of positive gain. The presence of many frequencies in the wave dynamics results in their nonlinear interaction. Thus, the overall picture is rather complicated. However, if we are interested in waves of the highest amplitude, the problem can be simplified and effectively reduced to the interaction of two independent frequencies within the positive-gain band.

It is well known that the nonlinear Schrödinger equation (Eq. (1), see below) has soliton solutions that are localized along the t axis. Solitons can exist on a zero background (completely localized) or on a plane wave background (Ma solitons [11]). Another limiting case is the one formed by solutions that are localized along the x axis ("Akhmediev breathers" [1,12–16]). These are always located on a plane wave background and represent a nonlinear stage of evolution of the modulation (Benjamin–Fair [17] or Bespalov–Talanov [18]) instability. Localization in the x-direction is just a manifestation of Fermi–Pasta–Ulam (FPU) recurrence for the NLSE-model [19,20].

Each class of the above-mentioned solutions is a particular case of a more general multi-parameter family of solutions that describe periodic waves in the x and t directions [21,22]. The interrelation between these solutions is schematically represented in Fig. 1. A more accurate representation can be found in Fig. 3.2 of Ref. [22]. This diagram shows that the Peregrine solution is a limiting case of a one-parameter family of Ma solitons and also of a one-parameter family of Akhmediev breathers (ABs). Likewise, a soliton solution is a limiting case either of a one-parameter family of cnoidal waves or Ma solitons, etc. Finally, all the above solutions are limiting cases of a two-parameter family of first-order solutions of the NLSE [21] that fill the entire triangle in Fig. 1 (see also Ref. [22, Chapter 3]). Generally speaking, this family consists of solutions which are periodic along both the x and t axes. When one of the periods tends towards an infinite value, we have the limiting case of either an ordinary soliton or the "Akhmediev breather". When both periods are infinite, then the general solution has, as a limiting case, the simplest rational solution or "Peregrine soliton". The latter is localized in both directions, x and t.

The "first-order solutions" are the lowest-order solutions that the NLSE admits (apart from the trivial zero solution). It is very unlikely that they can be observed in the ocean in pure form. The actual wave dynamics consists of a nonlinear superposition of many simple periodic solutions. Just as two-(or more)-soliton solutions are nonlinearly combined from one-soliton solutions, the multi-periodic solutions can be combined from the "first-order" ones. In particular, two "Peregrine solitons" can be combined into a single more complicated doubly-localized structure with a much higher amplitude [23,24]. The superposition of several simple periodic solutions can take the form of chaotic waves.

Now, the question is: what is a rogue wave? Is it just a single soliton, or a combination of several periodic solutions? When dealing with chaotic solutions, we are interested in the maximal

* Corresponding author.
E-mail address: iodsc09@io.cfmac.csic.es (J.M. Soto-Crespo).

0375-9601/$ – see front matter
doi:10.1016/j.physleta.2009.04.023

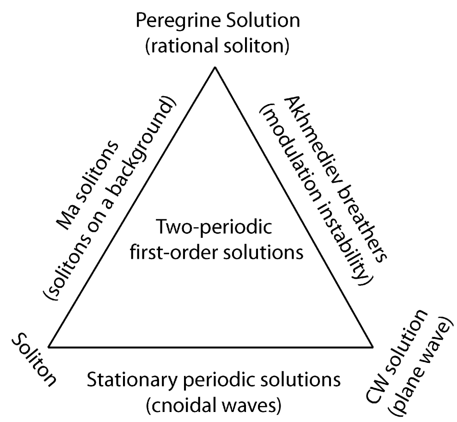

Fig. 1. Interrelation between various solutions of the NLSE.

amplitudes of the local field distribution. Supposedly, these local maxima are the rogue waves that appear in the ocean from time to time. In this Letter, we give a possible answer to the above question.

Indeed, waves in the ocean are chaotic. This means that their spectra contain a continuous range of frequencies. If we model the wave phenomena in the ocean by the NLSE, we have to take into account the multiplicity of frequencies that exist in the initial conditions. The self-focusing NLSE has a plane wave solution that is unstable relative to modulation instability. All frequencies that are in the instability band are amplified. After amplification, they reach their maximal amplitudes and then decay to zero [16]. Thus, their interaction can happen over a limited range of propagation distances, just like the interaction of two solitons. This means that for a relatively quiet ocean, and in order to observe the local maxima of the field, we can limit ourselves to the interaction of just two "Akhmediev breathers". A collision of three of them would be a relatively rare event. At the same time, these collisions happen again and again, thus producing many local maxima of the field. Indeed, there are many frequencies in a random initial condition and interactions between "Akhmediev breathers" of various frequencies are unavoidable. In this respect, we should mention that the situation is a little different from the collision of two Peregrine solitons. Each is localized in two directions, and so it would then be less likely to have two of them located in the same position. Additionally, they need longer distances to develop, since the growth rate for them tends to zero and these waves grow according to a power law.

To answer the question of what is the nature of rogue waves, we solved the NLSE with initial conditions in the form of a plane wave with a random modulation. Thus, all frequencies within the instability band will be amplified, but the overall maximum of the field remains limited. We investigated all local maxima of the generated field and chose the ones that have the highest amplitude at the crest. We then analyzed some absolute maxima and compared them with the result of exact solutions in the form of (i) the collision of two "Akhmediev breathers" and (ii) second-order rational solutions. Comparisons show clearly that all of these maxima can be interpreted in terms of the above collisions.

The results that we present in this Letter can equally well be applied to the ocean waves and waves in optical fibers [25,26]. In contrast to the undesirable rogue waves in the ocean [1,27], generation of high energy pulses is one of the ultimate goals of modern optics [28,29]. The knowledge of the mechanisms of creation of the rogue waves allows us to generate them deterministically rather than relying on chaotic initial conditions. Indeed, the first order solutions of NLSE or "Akhmediev breathers" have been already observed by Van Simaeys, Emplit and Haelterman [19]. Observation of higher order solutions is just a question of adding more harmonics into the initial modulation and adjusting properly the length of the fiber. Thus, from technical point of view this does not seem to be very difficult.

2. Numerical simulations with initial conditions in the form of a plane wave + random noise

The integrability of the nonlinear Schrödinger equation was discovered by Zakharov and Shabat [30]. As numerous applications were found, the equation became quite popular. In normalized form, it can be written as:

$$i\frac{\partial\psi}{\partial x}+\frac{1}{2}\frac{\partial^2\psi}{\partial t^2}+|\psi|^2\psi=0 \tag{1}$$

where x is the propagation distance and t is the transverse variable. This notation is standard both in nonlinear fiber optics [31] and in the theory of ocean waves [3]. Note that ψ represents the envelope of a physical solution, and, in optics, its squared modulus represents a measurable quantity, viz. intensity. For the ocean waves, we assume [14] that there is a carrier wave with wavelength $\lambda(\approx\omega^{-1})$ comparable to the central region of the envelope. So the actual water height, relative to the equilibrium sea-level, would be $|\psi|\cos(\omega t)$. The potential energy of a segment in t, of width Δt, is then proportional to $|\psi|^2\Delta t$. Therefore, this value for ocean waves acts like the intensity in optics.

We used, as the initial condition when solving Eq. (1), a plane wave with random noise superimposed on it, viz.

$$\psi(x=0,t)=\left[1+\mu f(t)\right] \tag{2}$$

where $f(t)$ is a normalized complex random function whose standard deviation is $\sigma=1/\sqrt{3}$. When multiplied by μ, this gives the standard deviation for the whole function (2). Deviations from the average amplitude, 1, can be relatively high. However, the spectral amplitudes at each frequency component are still very small in comparison with the zero spectral component. It is important that both real and imaginary parts of the function $f(t)$ are independent random variables, each with a Gaussian correlation function.

To be specific, the real and imaginary parts of $f(t)$ are constructed independently in the following way. The numerical discretization of either the real or imaginary parts of $f(t_k)$ is obtained from a sequence of random numbers uniformly distributed in the interval $[-1,1]$, correlated with a Gaussian, $(2/\sqrt{\pi}\tau)\exp[-2(k/\tau)^2]$. When $\tau=0$ in this expression, the random sequence is completely uncorrelated. When $\tau\neq 0$, the correlation is proportional to the mean width in the t-direction of the random waves. Initially, at the linear stage of evolution, the spectral components propagate with a variety of velocities, i.e. at almost any angle relative to the start line, $x=0$. As τ is inversely proportional to the width of the initial spectrum, the results of evolution should depend on whether this spectrum is wider or narrower than the spectral band of modulation instability. The latter is defined by the amplitude of the plane wave. In our case the amplitude is 1, so the spectral band for modulation instability is twice 2.

A typical example of the initial condition (2) is shown in Fig. 2. The spectrum of this initial condition is shown in Fig. 3(a). The component at $f=0$ has been removed from the figure as it exceeds the rest of the spectral components by several orders of magnitude. According to the above estimate, the initial spectrum is located completely within the spectral band of modulation instability, so that all spectral components will be amplified. The spectra at later stages of the evolution (see Fig. 3(b)) are wider due to the four-wave mixing processes. The initial field amplitudes are normalized to give a mean value of the field intensity

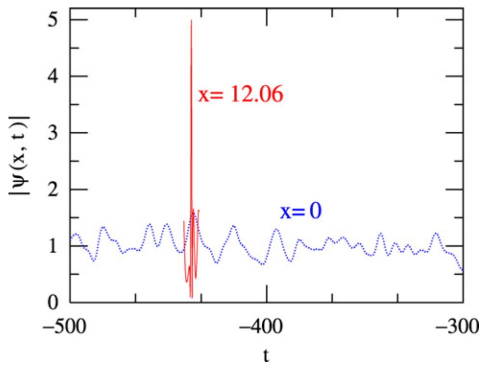

Fig. 2. Typical example of a small fraction of the initial condition (see Eq. (2)) in the form of a plane wave perturbed by a random function $f(t)$ (dotted blue line) with an amplitude of $\mu = 0.6$, where the mean width of the irregularities is $\tau = 3.9$. The full temporal interval is much wider and extends from $t = -1000$ to $t = 1000$. The red solid curve shows part of the field modulus, $|\psi|$, at $x = 12.06$ where it reaches its highest value, viz. 5. (For interpretation of the references to color in this figure legend, the reader is referred to the web version of this Letter.)

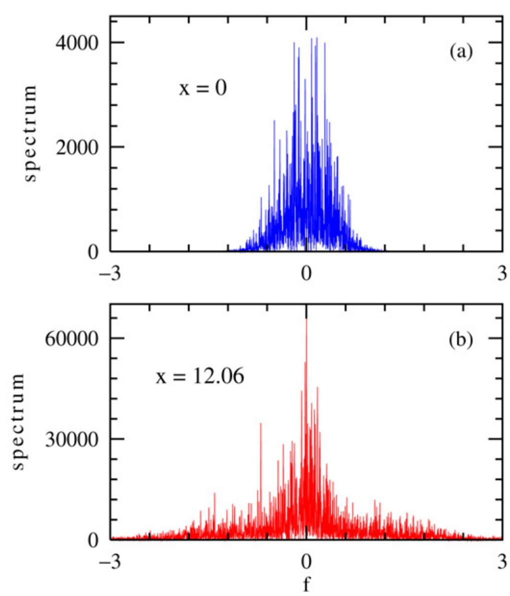

Fig. 3. Spectra of (a) the initial condition, and (b) the field at $x = 12.06$.

equal to 1, i.e. $\langle|\psi(0,t)|^2\rangle = 1$. As a consequence of the conservation of energy, this magnitude is a constant during the propagation.

Initially, each spectral component of the random perturbation within the instability band grows exponentially, but, at a later stage, we arrive at an average excited state of the ocean surface. Due to the recurrence phenomenon for each modulation instability wave [16], the field amplitudes remain finite. We are interested in the highest amplitudes of the resulting "ocean surface". In each numerical run, we singled out the maximum values of the field which can potentially be "rogue waves". Namely, at each x, we found the absolute maximum of the function $|\psi(x = \text{const}, t)|$ and plotted it against the x value. The corresponding plot for the initial condition presented in Fig. 2 is shown in Fig. 4. At some points, the maximum of the function can become the crest of the wave, i.e. a local maximum in the two directions, x and t. The highest maximum in the plot of Fig. 4 can be considered as the most ferocious "rogue wave". This happens, in this numerical example, at $x = 12.06$. The part of the field amplitude with this maximum is shown, in red, in Fig. 2. The position where the maximum appears is completely random, of course.

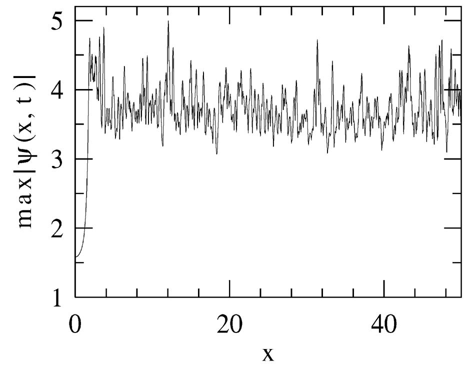

Fig. 4. The maximum of the chaotic field $\phi(t) = |\psi(x = \text{const}, t)|$ vs. propagation distance, x, for the case of the initial condition partially represented in Fig. 2. Note that the average amplitude of the two-dimensional field, $|\psi(x,t)|$, is around 1, i.e. it is much lower. The highest maximum in this simulation is 5. It appears at $x = 12.06$.

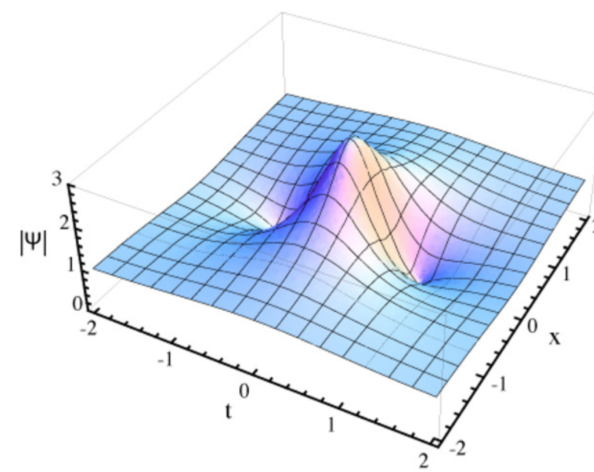

Fig. 5. First-order rational solution (Eq. (3)).

The highest amplitude that appears in this numerical run is close to 5. This amplitude cannot be associated with any of the first-order solutions since the maximum amplitude in that case is 3. The latter is attributed to the first-order rational solution (Peregrine soliton):

$$\psi = \left[1 - 4\frac{1 + 2ix}{1 + 4x^2 + 4t^2}\right]e^{ix}. \qquad (3)$$

This solution is shown in Fig. 5. All solutions in the present Letter are normalized in such a way that the starting plane wave has the amplitude equal to 1. Due to the conservation of energy, the average amplitude always remains equal to 1. Then the amplitudes at the wave crests are found relative to this value. This is important because all the exact solutions written below have the same reference background amplitude. The latter can be rescaled when necessary (see scaling transformation in [22]).

It is worth noting that 5 is exactly the amplitude of the second-order rational solution of the NLSE [24]. For the sake of completeness, we present this solution here:

$$\psi = \left[1 - \frac{G + iH}{D}\right]e^{ix} \qquad (4)$$

where G, H and D are given by:

$$G = -\frac{3}{16} + \frac{3}{2}t^2 + t^4 + \frac{9}{2}x^2 + 6t^2x^2 + 5x^4,$$

$$H = x\left(-\frac{15}{8} - 3t^2 + 2t^4 + x^2 + 4t^2x^2 + 2x^4\right),$$

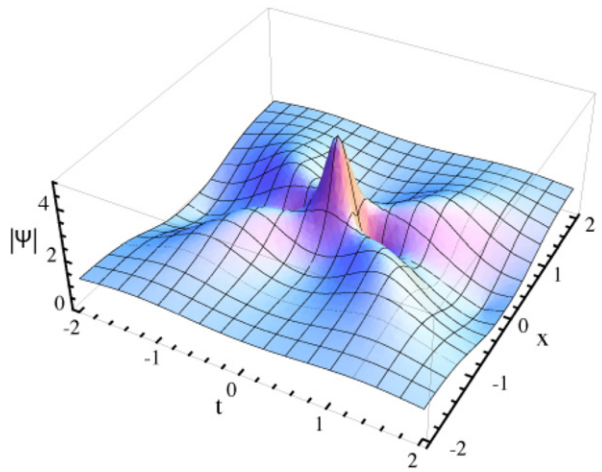

Fig. 6. Higher-order rational solution (Eq. (4)).

$$D=\frac{3}{64}+\frac{9t^2}{16}+\frac{t^4}{4}+\frac{t^6}{3}+\frac{33}{16}x^2-\frac{3}{2}t^2x^2 +t^4x^2+\frac{9}{4}x^4+t^2x^4+\frac{x^6}{3}.$$

This solution is shown in Fig. 6. Because its maximum amplitude is equal to 5, it can, in principle, explain the high amplitudes that we observed in the numerical simulations. However, we should take into account that this solution is a nonlinear superposition of two rational solutions of first-order. As each of them is localized both in x and t directions, their appearance at the same position simultaneously would be an extremely rare event. So, we have to look for other possibilities.

3. Akhmediev breathers and their collisions

As an alternative, we consider the collision of two ABs. These are extended in the t direction, so such a collision would have a higher chance of occurring in a chaotic wave field. In fact, the superposition of any two solutions close to the top of the triangle in Fig. 1 would result in a maximal amplitude close to 5. In order to construct this solution, we will use the Darboux transformation.

The condition of integrability of the NLSE is the compatibility of the two following linear equations:

$$\mathbf{R}_t=l\mathbf{JR}+\mathbf{UR},$$
$$\mathbf{R}_x=l^2\mathbf{JR}+l\mathbf{UR}+\frac{1}{2}\mathbf{VR}, \tag{5}$$

where $\mathbf{U}$, $\mathbf{J}$ and $\mathbf{V}$ are the following matrices:

$$\mathbf{U}=\begin{bmatrix}0 & i\psi^*\\ i\psi & 0\end{bmatrix},\qquad \mathbf{J}=\begin{bmatrix}i & 0\\ 0 & -i\end{bmatrix}, \tag{6}$$

$$\mathbf{V}=\begin{bmatrix}-i|\psi|^2 & \psi_t^*\\ -\psi_t & i|\psi|^2\end{bmatrix}, \tag{7}$$

while $\mathbf{R}$ is a column matrix

$$\mathbf{R}=\begin{bmatrix}r\\ s\end{bmatrix} \tag{8}$$

and l is a complex eigenvalue.

Eqs. (5) establish a one-to-one correspondence between the solutions of the NLSE and the solutions of the linear system. The linear system can be solved with ease for the case of trivial solutions of the NLSE such as the zero solution or the plane wave solution. In order to deal with more complicated solutions, we can start with one of the above as a "seeding solution" and use it in Darboux transformations to obtain more complicated ones. The zero solution allows us to construct the hierarchy of multi-soliton solutions [32], while the plane wave solution results in the hierarchy of solutions related to modulation instability [34].

The eigenvalue l in Eqs. (5) is practically an arbitrary complex number (within certain limits) that appears as the parameter of the family of solutions that are going to be constructed. In the case of the solutions related to modulation instability, the real part of the eigenvalue is the "velocity" of the solutions, i.e. the angle that the one-dimensionally localized solution forms with the x-axis, while the imaginary part characterizes the frequency of the periodic modulation. As we are going to build the solution that is a collision of two first-order breathers, we select two solutions of the family and thus we need two eigenvalues, i.e. $l=l_1$ and $l=l_2$. For higher-order solutions to exist, these eigenvalues have to be different.

Following Ref. [34], we shall assume that the seeding solution of the NLSE is a plane wave of amplitude 1, i.e.:

$$\psi_0=\exp(ix). \tag{9}$$

Two linear functions $r=r(x,t)$ and $s=s(x,t)$ that make the system (5) compatible with $\psi=\psi_0$ are

$$r=\big\{A\exp\big[i(2\chi+\kappa t+l\kappa x)/2\big] -B\exp\big[-i(2\chi+\kappa t+l\kappa x)/2\big]\big\}\exp(-ix/2),$$
$$s=\big\{A\exp\big[i(-2\chi+\kappa t+l\kappa x)/2\big] +B\exp\big[-i(-2\chi+\kappa t+l\kappa x)/2\big]\big\}\exp(ix/2) \tag{10}$$

where $\chi=\frac{1}{2}\arccos(\frac{\kappa}{2})$, $\kappa=2\sqrt{1+l^2}$ and A and B are constants of integration, where we can embed the arbitrary center (x_0,t_0) of the solution, namely

$$A=\exp\big[(+il\kappa x_0-i\kappa t_0-i\pi/2)/2\big],$$
$$B=\exp\big[(-il\kappa x_0+i\kappa t_0+i\pi/2)/2\big]. \tag{11}$$

The phase shifts of $\pi/4$ are added to center the solutions at the origin when the translation values are zero. Below, we shall assume, without loss of generality, that $x_0=0$ and $t_0=0$.

Substituting A and B into (10) we find:

$$r_1=\big\{\exp\big[(2i\chi_1+i\kappa_1 t-i\pi/2+il_1\kappa_1 x)/2\big] -\exp\big[(-2i\chi_1-i\kappa_1 t+i\pi/2-il_1\kappa_1 x)/2\big]\big\}\exp(-ix/2),$$
$$s_1=\big\{\exp\big[(-2i\chi_1+i\kappa_1 t-i\pi/2+il_1\kappa_1 x)/2\big] +\exp\big[(2i\chi_1-i\kappa_1 t+i\pi/2-il_1\kappa_1 x)/2\big]\big\}\exp(ix/2), \tag{12}$$

where $\kappa_1=2\sqrt{1+l_1^2}$, $\chi_1=\frac{1}{2}\arccos(\kappa_1/2)$. We have added the subscript 1 to r, s and to the rest of variables, as they refer to the eigenvalue $l=l_1$. For the second eigenvalue, $l=l_2$ (see below), all subscripts 1 have to be changed to 2.

The nontrivial solution that is found at the first step of the Darboux scheme is given by:

$$\psi_1=\psi_0+\frac{2(l_1^*-l_1)s_1r_1^*}{|r_1|^2+|s_1|^2}. \tag{13}$$

Substituting r_1 and s_1 into this equation is a straightforward procedure. Explicit forms are given in Appendix A. A typical solution obtained when the complex eigenvalue l has both real and imaginary parts being nonzero is shown in Fig. 7. As discussed above, the real part of l_1, here labelled v, is responsible for the velocity of the breather, i.e. it defines the angle between the line of maxima of the solution and the t-axis. Here, the peaks of this periodic solution are located at a finite angle to the t axis.

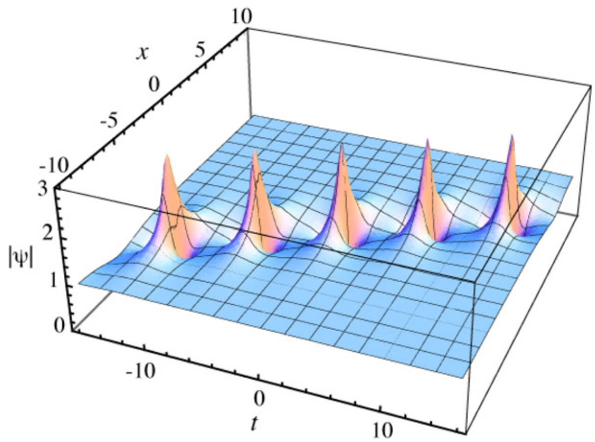

Fig. 7. Single Akhmediev breather with nonzero velocity (Eq. (13)). The eigenvalue is: $l_1 = 0.08 + i0.9$.

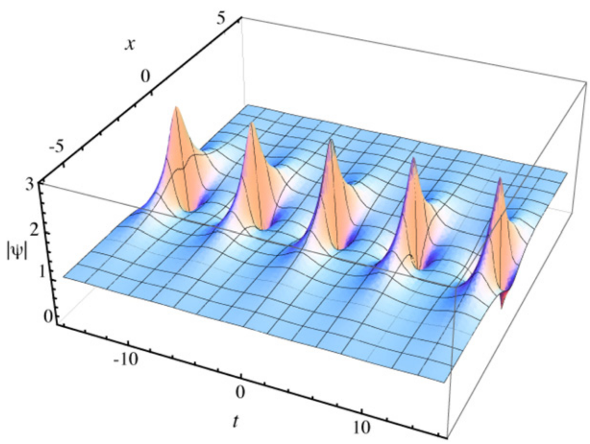

Fig. 8. Single Akhmediev breather with zero velocity (Eq. (14)). It corresponds to the eigenvalue $l_1 = i0.9$.

For a purely imaginary eigenvalue $l_1 = i\nu_1$, i.e. $l_{1i} = \nu_1$, we have $v = 0$, $d_{1r} = 0$, $\chi_{1i} = 0$ and $\kappa_{1i} = 0$ and we can further simplify the solution, as $\cos(2\chi_{1r}) = \kappa_{1r}/2$. We obtain:

$$\psi_1 = \left[1 - \frac{\kappa_1^2 \cosh\delta_1 x + 2i\kappa_1\nu_1 \sinh\delta_1 x}{2(\cosh\delta_1 x - \nu_1 \cos\kappa_1 t)}\right] \exp\left[i(x+\pi)\right], \tag{14}$$

where $\delta_1 = \nu_1\kappa_1$ and $\kappa_1 = 2\sqrt{1-\nu^2}$. It is shown in Fig. 8. Direct substitution shows that Eq. (14) satisfies the NLSE for all values of its parameter. This solution was found previously [16,21,23] using a different technique. The value of κ_1 defines the frequency of the modulation along the t-axis. It can change from zero to 2. This is the range of modulation instability, while $\delta_1 = \kappa_1\sqrt{1-\kappa_1^2/4}$ is its growth rate. Taking the limit as $\kappa_1 \to 0$ directly gives the first-order rational solution (3).

The higher-order solution that combines two independent frequencies of modulation, κ_1 and κ_2, can be found using the next step of the Darboux transformation. In order to do that, we use the solutions r and s with a different eigenvalue, $l = l_2$. The constants x_{02} and t_{02} are again taken as zero, $x_{02} = 0$, $t_{02} = 0$.

$$\begin{aligned} r_2 &= \left\{\exp\left[(2i\chi_2 + i\kappa_2 t - i\pi/2 + il_2\kappa_2 x)/2\right]\right. \\ &\quad \left. - \exp\left[(-2i\chi_2 - i\kappa_2 t + i\pi/2 - il_2\kappa_2 x)/2\right]\right\} \exp(-ix/2), \\ s_2 &= \left\{\exp\left[(-2i\chi_2 + i\kappa_2 t - i\pi/2 + il_2\kappa_2 x)/2\right]\right. \\ &\quad \left. + \exp\left[(2i\chi_2 - i\kappa_2 t + i\pi/2 - il_2\kappa_2 x)/2\right]\right\} \exp(ix/2). \end{aligned} \tag{15}$$

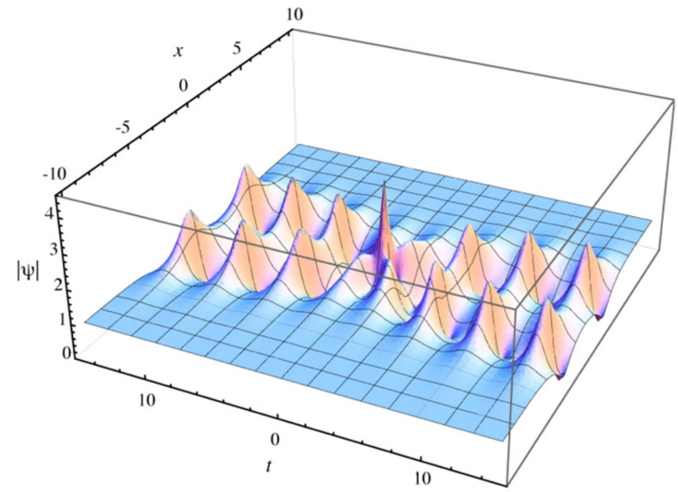

Fig. 9. Collision of two Akhmediev breathers with zero velocities (Eq. (17)). The eigenvalues are: $l_1 = i0.6$ and $l_2 = -i0.7$.

These linear functions produce a solution of the NLSE that is similar to (14). The solution of the linear set which corresponds to the higher-order NLSE solution can be written in terms of r_1, s_1, r_2 and s_2:

$$\begin{aligned} r_{12} &= \frac{(l_1^* - l_1)s_1^* r_1 s_2 + (l_2 - l_1)|r_1|^2 r_2 + (l_2 - l_1^*)|s_1|^2 r_2}{|r_1|^2 + |s_1|^2}, \\ s_{12} &= \frac{(l_1^* - l_1)s_1 r_1^* r_2 + (l_2 - l_1)|s_1|^2 s_2 + (l_2 - l_1^*)|r_1|^2 s_2}{|r_1|^2 + |s_1|^2}. \end{aligned} \tag{16}$$

The higher-order solution of the NLSE then is:

$$\psi_{12} = \psi_1 + \frac{2(l_2^* - l_2)s_{12}r_{12}^*}{|r_{12}|^2 + |s_{12}|^2}. \tag{17}$$

For the explicit form of (17) we refer to Appendix B.

This solution is shown in Fig. 9 for $\nu_1 = 0.6$ and $\nu_2 = 0.7$. Hence, the frequencies are $\kappa_1 = 1.6$ and $\kappa_2 = 1.43$. These frequencies are incommensurate. Thus, the superposition has one absolute maximum. With our choice of the integration constants, it is located at the origin. Even in this case, the central maximum of the solution is relatively high. It is certainly higher than the crests of other wavelets in the solution. This maximum will reach the value 5 when both κ's approach 1.

A typical higher-order solution for the case of complex eigenvalues is shown in Fig. 10. The eigenvalues here are: $l_1 = 0.05 + i0.9$ and $l_2 = -0.05 + i0.9$. The real part of each eigenvalue ± 0.05 is its "velocity". Thus, two ABs collide at a certain angle to each other. In this geometry, when the velocities are finite and different, the two breathers always collide in the space (x, t). Thus the probability of creating a rogue wave is much higher than in the case of the higher-order rational solution.

Qualitatively, the central part of the profile in each case looks very similar to the higher-order rational solution. This is not unusual because the rational solutions are limiting cases of the ABs in the infinite period limit. However, the probability of the overlapping in the two-dimensional space of the high-order rational solutions is very low, while ABs will necessarily collide, at least at one point. If they are moving with finite velocities, then their collision is very similar to the collision of two solitons, except for the direction of the localization and the periodicity of each breather.

4. Comparison of numerical simulations with the exact solutions

The above results show that it is indeed possible that "rogue waves" can be attributed to higher-order solutions. In order to

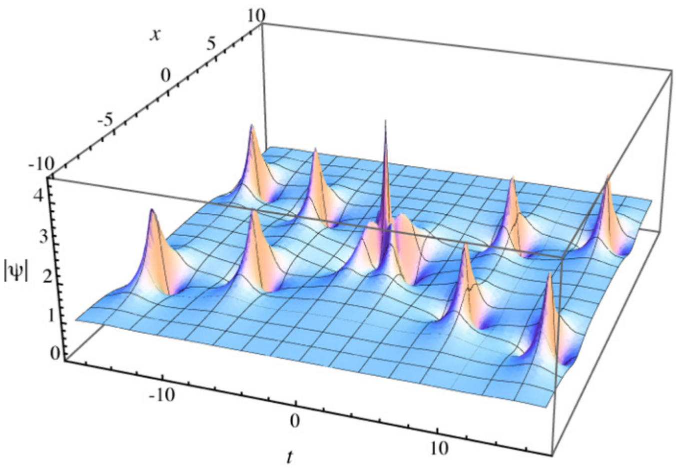

Fig. 10. Collision of two Akhmediev breathers with nonzero velocities (Eq. (17)). Eigenvalues are: $l_1 = 0.05 + i0.9$ and $l_2 = -0.05 + i0.9$.

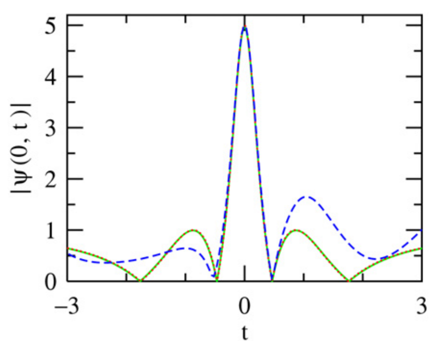

Fig. 11. (Dashed blue line) Amplitude profile of the chaotic wave along t around the point of the highest maximum amplitude in Fig. 4. It is compared with (dotted red line) the higher-order rational solution of the NLSE (Eqs. (4)) and (green solid line) with the collision of two ABs (Eq. (17)) with $l_{1,2} = \pm 0.05 + 0.99$. (For interpretation of the references to color in this figure legend, the reader is referred to the web version of this Letter.)

confirm this conclusion, we made a detailed comparison of the wave profile that appears in the simulations using random initial conditions with the exact profiles defined by the analytic solutions. These plots are presented in Figs. 11 and 12 along the t and x directions, respectively. In each plot, the dashed blue line is taken from the numerical simulations. The exact rational solution (Eq. (4)) is shown by the dotted red line, while the collision of two Akhmediev breathers is shown by the green solid line.

The conclusion is that the amplitude profile around the peaks indeed closely resembles both the second-order rational solution and the result of the collision of two ABs. The central part of the peak accurately follows each of the exact profiles. The discrepancy in the tails of the peak are due to random smaller amplitude waves surrounding the peak.

A qualitative description of the solution that starts with a random function on the top of a plane wave would be the following. As our model is integrable, the solution consists of the nonlinear superposition of first-order periodic waves (see Fig. 1), Akhmediev breathers, Ma solitons and Peregrine solitons. Periodic waves within and beyond the instability bandwidth maintain constant amplitude and comprise a background for soliton-like solutions. Soliton-like solutions have a chance to collide and increase the amplitude of the wave upon a collision. Rational solitons are localized in each direction. Their dynamics is relatively simple: they appear from nowhere and disappear keeping a fixed location (in the moving frame). Thus, the appearance of the higher-order rational solution has a very low probability. Consequently, we mainly have

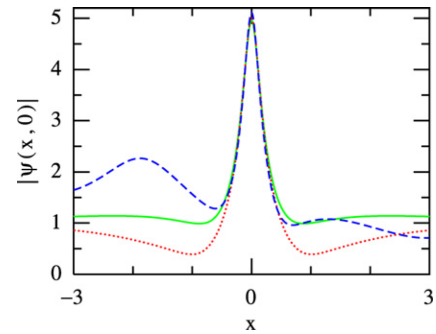

Fig. 12. Amplitude profiles around the highest maximum along the x-direction. The notations are the same as in Fig. 11.

to consider collisions of Ma solitons and Akhmediev breathers. Ma solitons are not created in our initial conditions, since we are considering relatively low amplitude perturbations to a plane wave. Thus, we are left with only collisions of ABs. The latter appear from small perturbations and reach finite amplitudes due to modulation instability somewhere in the middle of the simulations.

Generally, there would be many spectral components within the bandwidth with various small amplitudes for each component. Thus, each component will grow at a separate rate, creating ABs. The latter collide upon evolution, creating higher-order solutions, as shown in the previous section. The collision of each pair creates a maximum with the value of up to 5. Triple collisions may happen but they have much lower probability. If any wave is created with the amplitude higher than 5, it can be the result of a triple collision.

5. More detailed numerical simulations

In order to quantify the probabilities of appearance for various values of the maxima, we considered two different initial conditions. In each case, we used the common value of $\tau = 3.9$, but for μ, we used $\mu = 0.1$ in one case while $\mu = 0.6$ in the second one. For these two cases, we plotted the number of maxima appearing in each simulation within small fixed intervals of amplitude, namely 0.05. Only maxima above a lower limit of 1.5 were counted. The total number of maxima in each case equals 1.3 million. In order to reach these numbers, we used wide intervals along the t axis, in conjunction with long simulations over propagation distance, x. Each simulation was repeated 50 times with new initial conditions that correspond to the same values of τ and μ. These massive simulations allowed us to reach several thousands of maxima within each small segment of amplitudes.

The results are presented in Fig. 13. The gray area corresponds to the value $\mu = 0.1$ while the vertically hatched area stands for $\mu = 0.6$. For more clarity, the upper part of each histogram is colored (on-line only) in blue and red, respectively. The inset shows separately the part of the same curves corresponding to the highest values of the maxima. The vertical axis here is highly magnified in order to see the smaller number of maxima.

These results clearly show that higher initial amplitudes, μ, shift the probability of appearance of wave maxima to higher values. The highest amplitudes that we observed in the simulations with $\mu = 0.6$ are around 5. The absolute maximum is always limited – a result which agrees with the conclusions of reference [33]. This means that the collision of two ABs is sufficient to explain the appearance of rogue waves.

In order to look deeper into this problem, we separately studied the influence of the two parameters that fix the initial conditions that we are using, namely, the mean height (μ) and the mean temporal width (τ) of the initial waves. For each pair of values of these parameters, we repeated the above-mentioned process, with

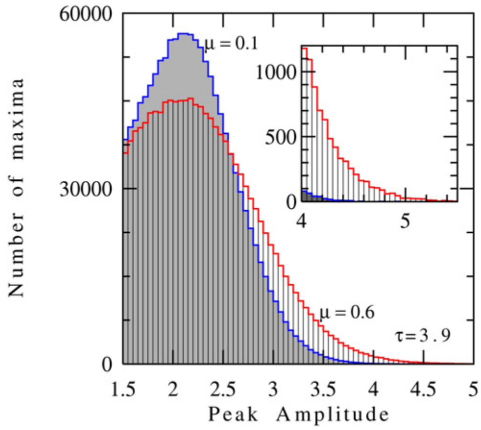

Fig. 13. The number of maxima in each segment of a particular wave amplitude for two simulations with different values of μ ($\mu = 0.1$ – blue line, gray area) and ($\mu = 0.6$ – red line, vertically hatched area). The inset shows a magnification of the same plot for higher values of the peak amplitude. Clearly, the peak amplitudes can reach higher values as μ increases. (For interpretation of the references to color in this figure legend, the reader is referred to the web version of this Letter.)

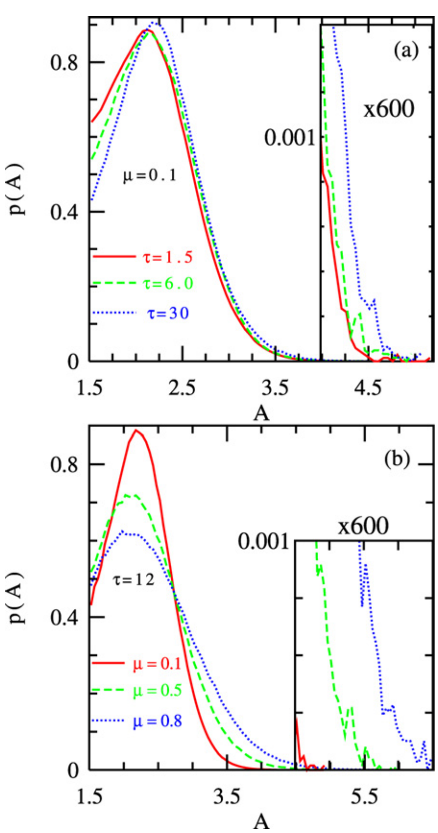

Fig. 14. Probability distribution of peak amplitudes for various values of (a) τ and (b) μ.

a number of realizations that was high enough to collect more than a million maxima for each case. The number of maxima in a certain interval around a given value of the amplitude (A), was divided by the length of the interval and the total number of maxima to obtain the corresponding density of probability, $p(A)$. These are presented in Figs. 14(a) and 14(b). In order to observe more clearly the probability of getting rogue waves, the region of high amplitude is magnified 600 times in the y-direction.

In Fig. 14(a), $\mu = 0.1$ and three different values of τ are considered. The red solid line is for $\tau = 1.5$, the dashed green line is for $\tau = 6$, and the dotted blue line is for $\tau = 30$. The maximum amplitudes in these cases are around 5. The probability of getting higher amplitudes increases as τ increases. Thus, when the initial excitation of the "ocean" is relatively low, the appearance of rogue waves can be completely explained by the collision of two ABs. The small difference in the probabilities for various values of τ can be explained by the different spectral components of the wave excitation falling within the modulation instability band. This becomes clear if we recall that the parameter τ, which describes the correlation length of the initial noise, is inversely proportional to the width of its spectrum.

In Fig. 14(b), we fixed $\tau = 12$, and dealt with three different values of μ. The red solid line is for $\mu = 0.1$, the green dashed line for $\mu = 0.5$, and the dotted blue line for $\mu = 0.8$. This plot once again shows a clear tendency to reach higher maximum amplitudes at larger values of μ. For $\mu = 0.5$ and 0.8, there are chances to observe the maxima around 5.5 and even 6.5. These amplitudes are clear evidence of the occurrence of triple AB collisions. Apparently, this can happen for highly excited states of the ocean surface, when the initial amplitudes of noise are comparable with the plane wave amplitude.

6. Conclusions

In conclusion, we have shown that when modeling chaotic waves in the ocean by the nonlinear Schrödinger equation, one of the possible explanations for the appearance of rogue waves is the collision of two Akhmediev breathers. Triple collisions can also be observed but their probability is much lower.

Acknowledgements

The work is supported by the Australian Research Council (Discovery Project scheme DP0985394). J.M.S.C. acknowledges support from the M.E.y C. under contract FIS2006-03376.

Appendix A. Explicit expressions for the solution of first-order

We can separate κ_j and χ_j (for $j = 1, 2$) into real and imaginary parts: $\kappa_j = \kappa_{jr} + i\kappa_{ji}$, $\chi_j = \chi_{jr} + i\chi_{ji}$. These are given explicitly:

$$\chi_{jr} = \frac{1}{2}\arccos\left(\frac{\kappa_{jr}}{p_j + q_j}\right),$$

and

$$\chi_{ji} = -\frac{1}{2}\operatorname{arccosh}\left(\frac{p_j + q_j}{2}\right),$$

where

$$p_j = \sqrt{\left(1 + \frac{\kappa_{jr}}{2}\right)^2 + \frac{\kappa_{ji}^2}{4}},$$

and

$$q_j = \sqrt{\left(1 - \frac{\kappa_{jr}}{2}\right)^2 + \frac{\kappa_{ji}^2}{4}}.$$

We can rewrite each function (Eq. (12)) r_1 and s_1 in terms of one trigonometric function with a complex argument:

$$r_1 = 2ie^{-ix/2}\sin(G), \qquad s_1 = 2e^{ix/2}\cos(H),$$

where

$$G = A_r + iA_i, \qquad H = B_r + iB_i,$$

with four real functions A_r, A_i, B_r, B_i which in turn are given by

$$A_r = \chi_{1r} + \frac{1}{2}(\kappa_{1r}t + d_{1r}x) - \frac{\pi}{4},$$
$$A_i = \chi_{1i} + \frac{1}{2}(\kappa_{1i}t + d_{1i}x),$$
$$B_r = -\chi_{1r} + \frac{1}{2}(\kappa_{1r}t + d_{1r}x) - \frac{\pi}{4},$$
$$B_i = -\chi_{1i} + \frac{1}{2}(\kappa_{1i}t + d_{1i}x).$$

Here $d_1 = d_{1r} + id_{1i} = l_1\kappa_1$, so $d_{1r} = \nu_1\kappa_{1r} - l_{1i}\kappa_{1i}$ and $d_{1i} = \nu_1\kappa_{1i} + l_{1i}\kappa_{1r}$.

Thus, we get:

$$\psi_1 = \left[1 + \frac{8il_{1i}}{D_1}\cosh(B_i - iB_r)\sinh(A_i + iA_r)\right]e^{ix}, \tag{18}$$

where

$$D_1 = \cos(2B_r) - \cos(2A_r) + \cosh(2A_i) + \cosh(2B_i). \tag{19}$$

For complex eigenvalue $l_1 = \nu_1 + il_{1i}$, we get

$$\psi_1 = \frac{F_1 + iF_2}{D_3}e^{ix} \tag{20}$$

where the real functions are given by:

$$F_1 = 2\cosh\big(\kappa_{1r}l_{1i}x + \kappa_{1i}(t + \nu_1 x)\big)\big(\cosh(2\chi_{1i}) - 2l_{1i}\sin(2\chi_{1r})\big)$$
$$\quad + 2\cos\big(\kappa_{1i}l_{1i}x - \kappa_{1r}(t + \nu_1 x)\big)\big(2l_{1i}\cosh(2\chi_{1i}) - \sin(2\chi_{1r})\big),$$
$$F_2 = 4l_{1i}\big(\cos(2\chi_{1r})\sinh(\kappa_{1i}t + \kappa_{1r}l_{1i}x + \kappa_{1i}\nu_1 x)$$
$$\quad - \sin\big(\kappa_{1i}l_{1i}x - \kappa_{1r}(t + \nu_1 x)\big)\sinh(2\chi_{1i})\big)$$

and

$$D_3 = 2\cosh(\kappa_{1i}t + \kappa_{1r}l_{1i}x + \kappa_{1i}\nu_1 x)\cosh(2\chi_{1i})$$
$$\quad - 2\cos(\kappa_{1r}t - \kappa_{1i}l_{1i}x + \kappa_{1r}\nu_1 x)\sin(2\chi_{1r}).$$

These equations can be simplified slightly more by noting that

$$\cos(2\chi_{1r}) = \kappa_{1r}/(p_1 + q_1)$$

while

$$\cosh(2\chi_{1i}) = (p_1 + q_1)/2.$$

However, this is not really necessary. Thus, we have the solution of the first order with nonzero velocity (20) in terms of real variables. When $\nu_1 = 0$, this solution reduces to Eq. (14).

Appendix B. Higher-order explicit solution

Just as for r_1 and s_1, we can rewrite the linear functions r_2 and s_2 using single trigonometric functions with a complex argument:

$$r_2 = 2ie^{-ix/2}\sin(C), \qquad s_2 = 2e^{ix/2}\cos(D),$$

where the arguments $C = C_r + iC_i$, $D = D_r + iD_i$, for real functions C_r, C_i, D_r, D_i which in turn are given by

$$C_r = \chi_{2r} + \frac{1}{2}(\kappa_{2r}t + d_{2r}x) - \frac{\pi}{4},$$
$$C_i = \chi_{2i} + \frac{1}{2}(\kappa_{2i}t + d_{2i}x),$$
$$D_r = -\chi_{2r} + \frac{1}{2}(\kappa_{2r}t + d_{2r}x) - \frac{\pi}{4},$$
$$D_i = -\chi_{2i} + \frac{1}{2}(\kappa_{2i}t + d_{2i}x),$$

where $d_2 = d_{2r} + id_{2i} = l_2\kappa_2$. Linear functions r_2 and s_2 can also be written in terms of trigonometric and hyperbolic functions of real arguments:

$$r_2 = \big[2i\cosh(m_2 + \chi_{2i})\sin(u_2 + \chi_{2r})$$
$$\quad - 2\cos(u_2 + \chi_{2r})\sinh(m_2 + \chi_{2i})\big]\exp\left(-\frac{ix}{2}\right),$$
$$s_2 = 2\big[\cos(u_2 - \chi_{2r})\cosh(m_2 - \chi_{2i})$$
$$\quad - i\sin(u_2 - \chi_{2r})\sinh(m_2 - \chi_{2i})\big]\exp\left(\frac{ix}{2}\right), \tag{21}$$

where $u_2 = (\kappa_{2r}t + d_{2r}x)/2 - \frac{\pi}{4}$ and $m_2 = (\kappa_{2r}t + d_{2i}x)/2$.

The higher-order solution of the NLSE is:

$$\psi_{12} = \psi_1 + \frac{2(l_2^* - l_2)s_{12}r_{12}^*}{|r_{12}|^2 + |s_{12}|^2} \tag{22}$$

where

$$r_{12}^* e^{-ix/2}D_1/2$$
$$= -4l_{1i}\cosh(B_i - iB_r)\cosh(D_i + iD_r)\sinh(A_i + iA_r)$$
$$\quad + \big[(\nu_2 - \nu_1 + il_{1i} - il_{2i})\big(\cos(2A_r) - \cosh(2A_i)\big)$$
$$\quad + (\nu_1 - \nu_2 + il_{1i} + il_{2i})\big(\cos(2B_r) + \cosh(2B_i)\big)\big]$$
$$\quad \times \sinh(C_i + iC_r)$$

and

$$s_{12}e^{-ix/2}D_1/2$$
$$= -4il_{1i}\cosh(B_i - iB_r)\sinh(C_i - iC_r)\sinh(A_i + iA_r)$$
$$\quad + \big[(\nu_2 - \nu_1 + il_{1i} + il_{2i})\big(-\cos(2A_r) + \cosh(2A_i)\big)$$
$$\quad + (\nu_2 - \nu_1 - il_{1i} + il_{2i})\big(\cos(2B_r) + \cosh(2B_i)\big)\big]$$
$$\quad \times \cosh(D_i - iD_r)$$

where D_1 is given by Eq. (19).

References

[1] C. Kharif, E. Pelinovsky, Eur. J. Mech. B (Fluids) 22 (2003) 603.
[2] P.A.E.M. Janssen, J. Phys. Oceanography 33 (2003) 863.
[3] M. Onorato, A.R. Osborne, M. Serio, S. Bertone, Phys. Rev. Lett. 86 (2001) 5831.
[4] V.E. Zakharov, J. Appl. Mech. Techn. Phys. 9 (2) (1968) 190. Originally in: Zh. Prikl. Mekh. Tekhn. Fiz. 9 (2) (1968) 86.
[5] V.I. Shrira, V.V. Georgaev, What makes the Peregrine soliton so special as a prototype of freak waves?, private communication, submitted for publication.
[6] A.R. Osborne, M. Onorato, M. Serio, Phys. Lett. A 275 (2000) 386.
[7] A.R. Osborne, Marine Struct. 14 (2001) 275.
[8] A.R. Osborne, Nonlinear Ocean Waves, Academic Press, 2009.
[9] P.K. Shukla, I. Kourakis, B. Eliasson, M. Marklund, L. Stenflo, Phys. Rev. Lett. 97 (2006) 094501.
[10] D.H. Peregrine, J. Australian Math. Soc., Ser. B 25 (1983) 16.
[11] Ya.-C. Ma, Stud. Appl. Math. 60 (1979) 43.
[12] A.A. Kurkin, E.N. Pelinovsky, Killer-waves: Facts, Theory and Modeling, Nizhny Novgorod Univ. Press, Nizhny Novgorod, 2004 (in Russian).
[13] K.B. Dysthe, K. Trulsen, Phys. Scr. T 82 (1999) 48.
[14] I. Ten, H. Tomita, Simulation of the ocean waves and appearance of freak waves, Reports of RIAM Symposium No. 17SP1-2, Proceedings of a symposium held at Chikushi Campus, Kyushu University, Kasuga, Fukuoka, Japan, 10–11 March 2006.
[15] V.V. Voronovich, V.I. Shrira, G. Thomas, J. Fluid Mech. 604 (2008) 263.
[16] N. Akhmediev, V.I. Korneev, Theor. Math. Phys. 69 (1986) 1089 (translation from Russian).
[17] T.B. Benjamin, J.E. Feir, J. Fluid Mech. 27 (1967) 417.
[18] V.I. Bespalov, V.I. Talanov, Zh. Eksp. Teor. Fiz. Pis'ma Red. 3 (1966) 471, English translation: JETP Lett. 3 (1966) 307.
[19] G. Van Simaeys, Ph. Emplit, M. Haelterman, Phys. Rev. Lett. 87 (2001) 033902.
[20] N. Akhmediev, Nature 413 (6853) (2001) 267.
[21] N. Akhmediev, V.M. Eleonskii, N.E. Kulagin, Theor. Math. Phys. 72 (1987) 809 (translation from Russian).
[22] N. Akhmediev, A. Ankiewicz, Solitons: Nonlinear Pulses and Beams, Chapman and Hall, London, 1997.
[23] N. Akhmediev, V.M. Eleonskii, N.E. Kulagin, Sov. Phys. JETP 62 (1985) 894.
[24] N. Akhmediev, A. Ankiewicz, M. Taki, Phys. Lett. A 373 (2009) 675.

[25] D.R. Solli, C. Ropers, P. Koonath, B. Jalali, Nature 450 (2007) 1054.
[26] D.-I. Yeom, B. Eggleton, Nature 450 (2007) 953.
[27] A.I. Dyachenko, V.E. Zakharov, JETP Lett. 88 (2008) 358.
[28] A. Fernandez, T. Fuji, A. Poppe, A. Fürbach, F. Krausz, A. Apolonski, Opt. Lett. 29 (2004) 1366.
[29] J.M. Dudley, G. Genty, B. Eggleton, Opt. Express 16 (2008) 3644.
[30] V.E. Zakharov, A.B. Shabat, Sov. Phys. JETP 34 (1972) 62.
[31] A. Hasegawa, F. Tappert, Appl. Phys. Lett. 23 (1973) 142.
[32] N. Akhmediev, N.V. Mitskevich, IEEE J. Quantum Electron. 27 (1991) 849.
[33] M. Tanaka, Wave Motion 12 (1990) 559.
[34] N. Akhmediev, V.I. Korneev, N.V. Mitskevich, Zh. Teor. Eksp. Fiz. 94 (1988) 159, JETP 67 (1988) 89.